Performance and Secondary Flow Structures Characterization in a Highly Loaded Low-Pressure Compressor Under Distorted Inflow Conditions

Riccardo Toracchio[1,*], Koen Hillewaert[2], Fabrizio Fontaneto[1]

[1]von Karman Institute for Fluid Dynamics, B-1640 Rhode-St-Genèse, Belgium
email: riccardo.toracchio@vki.ac.be, fabrizio.fontaneto@vki.ac.be

[2]University of Liège, 4000 Liège, Belgium
email: koen.hillewaert@uliege.be

ABSTRACT

A highly-loaded 1.5-stage axial compressor representative of the first stage of a modern booster was tested in the von Karman Institute (VKI) R4 facility with an inlet total pressure distortion replicating realistic engine installation effects. Given the significant impact of the distortion on the stage operability, the flow features responsible for the observed performance loss were identified and characterized. To this end, time-averaged and time-resolved measurements were employed to gain a comprehensive understanding of the involved physical phenomena. Additionally, full-annulus URANS simulations were performed to characterize the distortion transfer mechanisms and the flow reorganization.

Unlike typical cases where the intensification of secondary flows leads to a reduction of stability and performance, the present stage responded unexpectedly to the inlet distortion, exhibiting an increased stall margin compared to the clean machine. Beyond the clean stall boundary, a significant performance reduction was observed in distorted conditions, yet without the onset of rotating stall. This behaviour was attributed to the propagation of critical flow structures within the distorted region and to a severe flow redistribution taking place after the distortion screen.

Keywords: Compressor, Distortion, Experiments, Unsteady CFD, Secondary flows

1. Introduction

Engine performance can be compromised by operations conducted at high inlet incidence for short-duration maneuvers, such as take-off, climb or crosswind [1]. Under these conditions, the flow may accelerate over the lip to supersonic speeds, causing boundary layer separation and the introduction of a distorted inflow at the engine inlet. This effect is particularly critical for short intakes, which suffer from reduced diffusion capabilities [2,3], and can propagate within the engine, affecting downstream components like the low-pressure compressor. Also the theoretical advantages of modern aircraft architectures, such as Boundary Layer Ingestion (BLI), could be jeopardized by the development of a distorted flow at the engine inlet [4,5].

The impact of inlet distortions on the performance and stability of certain compressors is fairly understood. In [6], the authors analysed a low-speed BLI fan rig with an inlet rectangular distortion of 60°. A stage total-to-total efficiency drop of 5.3\% was respectively measured with respect to the design conditions. The same test-article was used to analyse the stall inception mechanisms under a typical BLI inlet profile [7], and it was found that the distortion was promoting a reduction in stability margin of 1-2% in terms of flow coefficient. The impact on the performance of a NACA-65 compressor rotor from different types of total pressure distortions was assessed numerically in [8]. The authors observed a consistent reduction of stage pressure ratio and efficiency for all distortions patterns with respect to the clean conditions. Although numerous studies in the literature examine the impact of inlet distortions on performance, most of this research primarily concentrates on fans, due to their critical role in the definition of the overall aircraft propulsive performance, or on standard compressor and fan geometries (e.g., NASA rotor 37 and NASA rotor 67 [9,10]). Moreover, canonical distortion patterns, such as rectangular configurations with the pressure deficit confined to a specific angle sector, are frequently analyzed in the literature.

For instance, in [11-14] the effects of 60°, 120° and 180° total pressure distortions on the NASA Rotor 67 fan stage and the TUD-R1 compressor, operated at TU Darmstadt, were examined. The Rotor 67 was analysed numerically under a 120° distortion in [15,16], showing that the stall margin loss increases at reduced speeds for a fixed distortion strength. The authors concluded that the radial loading distribution impacts the total pressure loss during stall, and a reduced tip loading would help limiting these losses. Moreover, while the distortion alters the stall process of the fan, stable rotating stall retains the same number, size and speed of stall cells. More representative distortion profiles, such as those of a BLI configuration, were examined for the NASA 67 rotor fan [17]. As the rotor moved out of the distorted region, where inlet incidence increases, the tip leakage flow-shock interaction intensified, causing the vortex breakdown and enhanced losses. Similar findings were reported in [18] for the TUD transonic compressor with a 120° tip distortion over 10\% span. Experimental and numerical analyses on a low-speed fan replicating realistic BLI distortions [19] showed that the flow redistribution within the low-pressure hub region increased local loading and work, reducing the overall efficiency. Earlier studies on transonic compressors and canonical geometries (e.g., NASA rotor 37) are available in [20-23], despite many other works can be found in the literature.

However, these designs, along with most of those present in the literature, differ substantially from modern boosters in both aerodynamic and structural aspects (such as blade solidity, aspect ratio, and loading) and the distortions analyzed often do not adequately represent real engine configurations. A comprehensive investigation is still required, particularly regarding the identification of the flow drivers and mechanisms contributing to the performance and stability modification in modern low-pressure compressors subjected to engine-representative distortions.

To this end, experiments were conducted at the von Karman Institute for Fluid Dynamics on a modern highly-loaded booster, operated for the first time with distorted inlet flows representative of real engine installation effects. In this context, the impact of the distortion on the stage performance and operability was different than expected. An increase of stall margin was indeed observed, yet with a performance reduction compared to the clean machine. This was attributed to the development of enhanced flow structures within the highly distorted regions of the annulus and to significant flow redistributions. The primary objective of this paper is therefore to provide a thorough understanding of the critical flow features responsible for modifications in stage operability and examine their evolution relative to the clean case.

This paper is structured as follows: the distortion considered is first introduced, followed by a description of the experimental and numerical environments. The operating points selected for this study are discussed, along with the design and installation of the distortion screen. The performance is then analyzed to assess modifications in stage operability compared to the clean case. The secondary flows contributing to the observed behavior are finally characterized experimentally, and the results of 3D URANS full-annulus simulations are presented to support this understanding and provide a simplified representation of the distortion transfer and of the annular flow redistribution.

2. Reference distortion

The distortion considered in this study corresponds to the fan outlet flow field in a geared ducted Ultra-High Bypass Ratio (UHBR) ($12 < BPR < 20$) turbofan engine. It replicates the circumferential total pressure distribution observed in fan-intake interactions during crosswind operations [24]. This distortion pattern was chosen for its relevance to modern engine designs but also because it refers to a particularly severe engine operation that may emphasize the distortion impact. No radial, swirl, and total temperature distortions are considered.

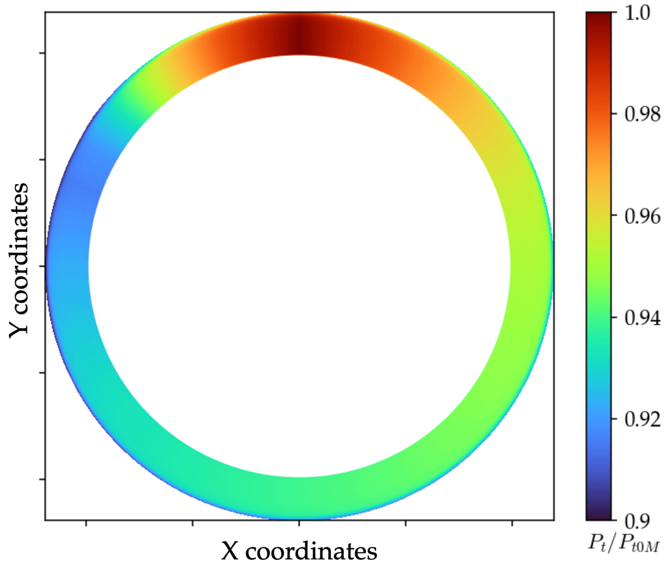

Figure 1 Reference total pressure distortion representative of a UHBR turbofan operated in crosswind conditions [24].

It was then scaled to match the inlet conditions of the compressor under investigation, while preserving the same intensity of the original distortion. The total pressure variation is shown in Figure 1, expressed relative to the stage inlet total pressure measured in clean conditions (Pt_{0M}). This pattern corresponds to a 1 Engine-Order (EO) distribution, with a clean inlet section corresponding to the maximum pressure region.

Even though this study focuses mainly on UHBR engines operating in crosswind conditions, the results are expected to be relevant for the entire engine community working on distortions, including BLI and Short Nacelle High Bypass (SNHB) turbofan applications, where distortions could significantly impact the engine performance and stability.

3. Experimental apparatus

3.1. Compressor test-article and VKI-R4 facility

This compressor stage was designed by Safran Aero Boosters (SAB) as a research stage to investigate highly-loaded geometries and identify limiting loading conditions for the next generation of boosters. In modern compressor geometries, indeed, enhancing the blade loading is essential to increase the pressure ratio while maintaining a compact core size [25]. In the particular case of the booster stage, where a fan-root distribution was considered, this resulted in a loaded hub section for the rotor.

It is a 1.5-stage characterized by an Inlet Guide Vane (IGV) row with 100 vanes, a rotor with 76 blades, and a stator with 100 vanes. The rotor features a hub-to-tip ratio of 0.82 and an inlet relative Mach number of approximately 0.75 at the tip, with a nominal rotational speed of 8748 rpm. The fixed-stagger IGV was designed to replicate the span-wise flow angle distribution typically observed at the outlet of a fan. Table 1 presents the design and flow parameters of the stage, while Figure 2 provides its sectional view, highlighting the axial measurement planes (0, 1, 2, 3, and 4). The large hub loading and the high Degree of Reaction (DOR) emphasize the significant aerodynamic loading of the rotor blade, making this compressor representative of a modern engine booster.

Design parameters	**Values**
IGV/rotor/stator blade count	100/76/100
R/S hub to tip ratio	0.82, 0.85
R/S aspect ratio	1.52, 1.51
R/S solidity	1.35, 1.81
Tip gap [span %]	0.8
Flow parameters	**Values**
Work coefficient	0.5-0.75 at hub
Flow coefficient	0.85-0.95 at hub
Degree of reaction	0.86 at mid-span
Tip relative Mach	0.75
Net aero-power [kW]	240

Table 1 Compressor design and flow features.

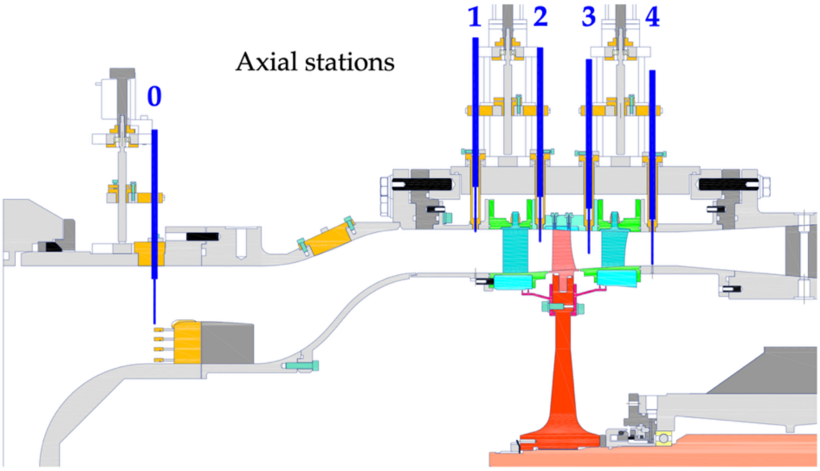

Figure 2 Compressor test-article.

This compressor stage is installed in the von Karman Institute high-speed compressor test rig R4 (Figure 3). The facility includes: 1) A reservoir tank; 2) The compressor test article; 3) A discharge collector; 4) A return duct that redirects the air back to the tank; and 5) A throttling valve for a precise control of the operating point. The rotor is powered by a 700 kW DC motor with controlled rotational speed. The closed-loop design allows for the pressure adjustment between 0.3 and 3 bars, while a heat exchanger in the settling chamber maintains the total inlet temperature within ± 1°C accuracy. This configuration enables an independent adjustments of the Reynolds and Mach numbers, allowing for the precise replication of specific aircraft flight conditions, such as cruise (CR) or take-off (TO).

Further details on the present stage and facility, operated in clean conditions with no inlet distortion, can be found in [26–29].

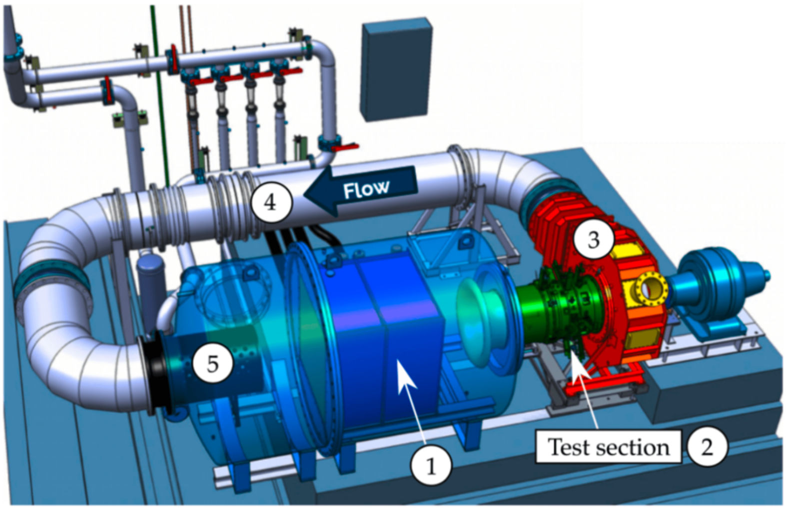

Figure 3 von Karman Institute R4 facility: closed-loop high-speed compressor test rig.

3.2. Operating conditions of interest

For the present work the set of speeds corresponding to 60%, 70%, 80%, 85%, 90%, 96% and 100% of the nominal speed was acquired for the characterization of the performance. However, a detailed description of the machine is provided only at 100% speed, as it corresponds to the condition of higher rotor inlet incidence, therefore more prone to the development of critical secondary flow structures. This is true especially in presence of the distortion that alters the inlet conditions of the stage.

For the detailed analysis of the flow field, two operating points are considered: Near-Stall (NS) and DEsign (DE). The NS condition is identified by the last point on each speed line before the appearance of an abrupt performance drop for both the clean and the distorted configuration. The DE operating point, instead, is identified by a specific corrected mass-flow and does not correspond to the point of maximum efficiency of the stage. Specifically, in the distorted case, an operating point with a mass-flow approximately between the clean and distorted stall boundaries was considered. This choice was taken to investigate an operating condition beyond the clean stability limit. These operating conditions will be referred to as ($DE_{c,e}$, $NS_{c,e}$) and ($DE_{d,e}$, $NS_{d,e}$) for the clean and the distorted case respectively (Table 2).

Speed	**EXP*clean***	**EXP*dist***
100 %	10.00 kg/s ($DE_{c,e}$)	8.45 kg/s ($DE_{d,e}$)
	8.90 kg/s ($NS_{c,e}$)	7.42 kg/s ($NS_{d,e}$)

Table 2 DE and NS corrected operating points analysed for the experimental clean and distorted configuration at 100Nn.

The absolute mass-flow of these operating points is [11.45, 10.04, 9.04, 7.96] kg/s for the DEc,e, NSc,e, DEd,e and NSd,e operating points, respectively.

Experiments have been performed at a single Reynolds number corresponding to atmospheric inlet conditions.

3.3. Distortion screen design and installation

The distortion screen design relied on procedures outlined in the literature for distortion gauze [30,31], but including different assumptions and considerations. The design process went through the following steps:

Step 1: A local evaluation of the total pressure loss coefficient ($K\ (\theta)$) was carried out using the difference between the clean pattern (P_c) and the distorted one to replicate ($P_d\ (\theta)$), as reported in Equation 1. Since the distortion is only circumferential, variations were considered exclusively as a function of the azimuthal position (θ). The inlet dynamic pressure (P_{dyn}) was derived from simulations conducted in clean conditions.

$$K\,(\theta) = \frac{Pc\ -\ Pd\,(\theta)}{Pdyn} \qquad (1)$$

$$KC\,(\theta) = 6.5 * \frac{1\ -\ \beta(\theta)}{\beta(\theta)^2\sqrt[3]{Redw\,(\theta)}} \qquad (2)$$

Step 2: Using correlations for mesh wires ($K_C\,(\theta)$ in Equation 2 [30]), the required set of loss coefficients to replicate the reference distortion was calculated. In this equation, $\beta(\theta)$ represents the screen porosity, and $Re_{dw}\,(\theta)$ is the Reynolds number based on the wire diameter (dw).

Step 3: The reference distortion was divided into discrete sectors. The range of identified $K_C\,(\theta)$ was divided into n = 4 user-defined sectors ($K_d\,(\theta) = range(K_C\,(\theta))/n$). Each point in the $K_C\,(\theta)$ distribution was replaced with the nearest $K_d\,(\theta)$ value to determine the extent of each sector.

Figure 4 presents the outcomes of Step 1, Step 2 and Step 3, in terms of retrieved total pressure, along with the final manufacturing of the screen, shown from a front view of the stage. In the picture, the clean section is located at 0° with respect to the absolute frame of reference of the stage and it corresponds to the region of maximum inlet total pressure (i.e. no pressure loss introduced by the screen). The rotor direction (ROT) is also shown to clarify the distortion distribution. This angle convention will be applied to all subsequent figures of the paper.

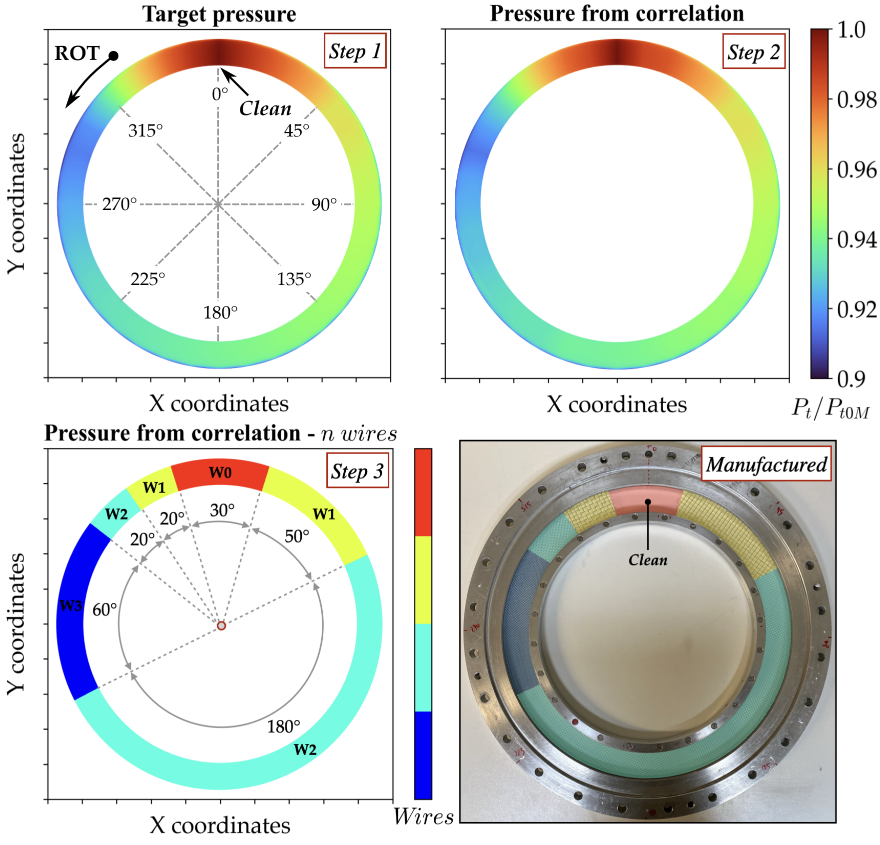

Figure 4 Distortion screen design.

The distortion screen was installed immediately upstream of experimental Plane 1 (IGV inlet) to: 1) Minimize the dissipation of the distortion before reaching the IGV, to closely replicate the target pattern; 2) Ensure a modular installation with minimal modifications to the existing stage components; 3) Ensure a configuration similar to that of the simulations, characterized by distorted inlet conditions applied in Plane 1. The installation of the screen immediately upstream of Plane 1 is expected to result in a minimal distortion dissipation as the distance between the screen and Plane 1 corresponds to $0.1D$, with D being the stage casing diameter.

Figure 5 reports the meridional view of the compressor with the placement of the distortion screen. As shown in the picture, the distortion screen consists of three components, labeled 1, 2, and 3, each holding meshes with varying porosities and wire diameters. These components are assembled prior to installation in the machine and are placed between the parts F1 and F2. Component 1 is fixed in the circumferential direction, while Components 2 and 3, along with the wire meshes, can be freely rotated within Component 1, providing a high resolution in the circumferential direction.

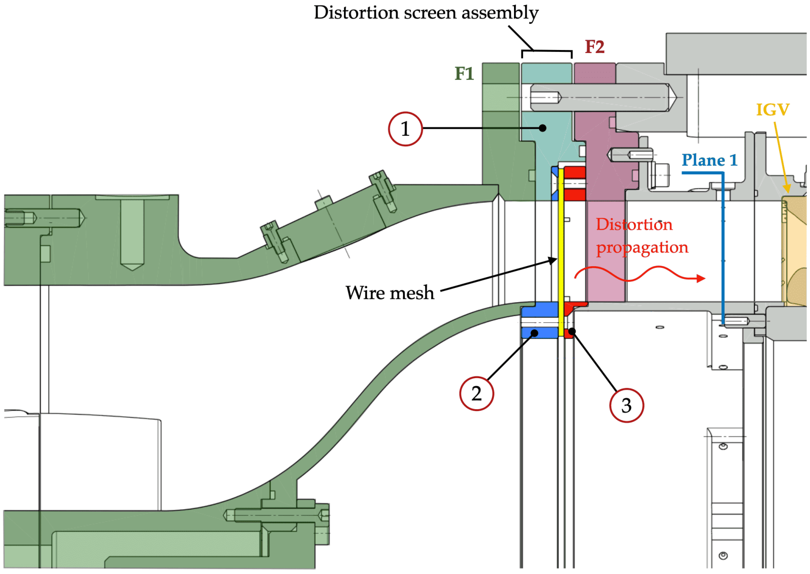

Figure 5 Sectional view of the compressor and positioning of the distortion screen assembly upstream of the measurement Plane 1.

3.4. Steady and unsteady instrumentation

Axial measurement planes are reported in Figure 2 with the following notation: Plane 0 (stage inlet), Plane 1 (IGV inlet), Plane 2 (IGV outlet/Rotor inlet), Plane 3 (Rotor outlet/Stator inlet), and Plane 4 (stage outlet). For each measurement plane, four azimuthal accesses (0°, 90°, 180°, 270°) can be used for the radial traversing of probes.

In Plane 1, located downstream of the screen, a 3-hole virtual pneumatic pressure probe was used for the distortion characterization. The latter consists in a single-hole probe, which is rotated around its axis to virtually simulate the presence of three holes, thereby enabling the reconstruction of flow quantities beyond the total pressure (such as static pressure, Mach number, and flow angle), as in a multi-hole probe but under the assumption of periodic steady flow. The methodology followed for the virtual operation of the probes is the one reported in [32]. In Plane 3 (rotor outlet) instead, a 3-hole virtual fast-response probe and a thermocouple probe were employed to measure the total pressure and total temperature at the rotor outlet. In Plane 4, a second pneumatic probe was installed for the description of the stage outlet flow field. All probes were installed facing the direction of the averaged flow field. Regarding the geometrical features, the pneumatic and the fast-response probes share the same design, featuring a 2 mm cylindrical head to reduce intrusiveness. The thermocouple junction was shielded to limit the sensitivity to flow angle variations. Figure 6 shows the pneumatic and thermocouple probes used in this measurement campaign.

Specifically, the fast-response probe was designed around a Kulite XCQ-SL-062 pressure transducer, and employs an active compensation scheme for the temperature given its superior performance in pressure readings than the passive approach [33]. It allowed the reconstruction of the Phase-Locked-Average (PLA) and of the Root-Mean-Square (RMS) of the pressure fluctuation in the rotor frame of reference, performing an acquisition at a sampling rate of 500kHz. This probe was also used to retrieve averaged span-wise distributions in Plane 3.

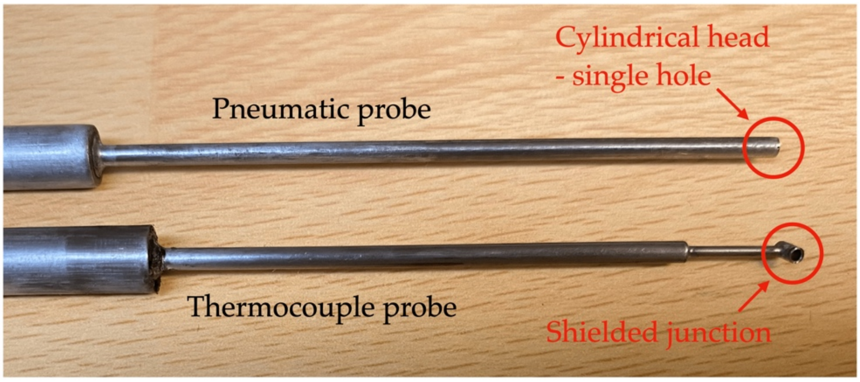

Figure 6 3-hole virtual pneumatic pressure probe and thermocouple probe.

Static pressure taps, total pressure rakes, and pneumatic probes were acquired using Scanivalve pressure scanners referenced to the inlet total pressure. A 2.5 PSI scanner was used in Plane 0 and 1, while a 15 PSI scanner was considered in Plane 4 to ensure good sensitivity. In the distorted configuration, a 5 PSI scanner was required in Plane 1 due to the pressure drop introduced by the screen. The scanners were referenced using a Keller PAA-33X absolute pressure sensor. Temperatures were instead acquired through a Scanivalve DTS3250 temperature scanner, to which all thermocouples (rakes and individual thermocouple probes) were connected.

All probes were traversed from 2.5% up to 97.5% span to avoid the probe heads colliding with the end-walls. The uncertainty computed with the ASME method [34] and expressed within the 95% confidence interval in the worst case scenario for the fast-response (FR), pneumatic (PN) and thermocouple (TC) probes are reported in Table 3. Pressure and temperatures are expressed relative to the measured inlet stage conditions.

UNC	PT	PS	Ma	Yaw	T
FR	±0.27%	±0.22%	±0.016	±0.8°	-
PS	±0.33%	±0.24%	±0.013	±0.6°	-
TC	-	-	-	-	±0.25%

Table 3 Propagated uncertainties for the fast-response (FR), pneumatic (PN) and thermocouple (TC) probes.

Tangential traversing, used to retrieve maps in the stage absolute frame of reference (e.g., Plane 4), was obtained by rotating the outlet stator row, while keeping the probe fixed. In this procedure, the clocking between IGV and outlet stator is not altered by means of a synchronized rotation of these components, which does not modify their relative position.

For the performance computation (pressure ratio, isentropic efficiency and temperature ratio), in Plane 0 four rakes are distributed over the annulus uniformly, while at the outlet (Plane 4), four rakes are arranged to span one stator pitch to retrieve a representative average of the outlet quantities. Six total pressure/total temperature Kiel heads are positioned on every rake at radii corresponding to the centers of equivalent areas. Moreover, eight static pressure taps uniformly distributed around the annulus in Plane 0 on the hub and tip walls, were employed. A linear span-wise static pressure interpolation enabled, together with the acquistion performed with the Kiels, the computation of the mass-flow. The performance was recorded with a sampling rate of 2Hz. The uncertainties for the corrected mass-flow, pressure ratio, temperature ratio and efficiency, expanded to a 95% confidence interval, were computed to be ± 0.078kg/s, ± 0.00071, ± 0.00245 and ± 2.0% at DE condition.

Finally, to retrieve the circumferential distribution of all quantities in distorted conditions, probes were kept fixed while the distortion screen was rotated by steps of 45°.This was performed by opening the rig and manually rotating the screen.

4. Numerical apparatus

In the framework of the present study, simulations were performed alongside experiments, for which only the corresponding mass-flow, retrieved from the performance analysis, was available. The simulations are therefore not intended to replicate the realistic experimental environment and operating points but rather to support the understanding of the annular flow redistribution at an operating point lying near the clean stall boundary. The present setup and mesh were validated under clean conditions in [26,35].

4.1. Numerical domain and mesh

A 3D full-annulus domain was considered to carry out the simulations reported in this paper. The inlet section was positioned at the location of measurement Plane 1, immediately downstream of the distortion screen in the actual test-section. The outlet section, instead, was placed 1.1 times the stator axial chord downstream of the exit measurement plane to avoid any potential influence of the outlet boundary condition on the results at the location of experimental Plane 4. At this location, the channels of the full-annulus domain were grouped into a single patch to allow the mass-flow redistribution across the annulus.

Technological features, such as fillets, were included in the numerical domain, while rotor/stator cavities present in the actual test-stage were excluded, as they are closed and believed to have minimal impact on the results [36,37]. The rotor tip gap was set to the averaged measured value.

The multi-block structured mesh was generated using Autogrid5 and IGG softwares. A Grid Convergence Index (GCI) analysis [38,39] was performed but not reported here for the sake of space. However, this mesh results from a minor modification of the grid reported in [26], which was shown to be representative of the experimental results while reducing the computational cost of the simulations. The final full-annulus mesh consists of a total of 140 million cells. An O4H symmetric B2B topology was applied to each blade row, and a OH topology was employed in the rotor tip gap region, with matching connections imposed at the periodic boundaries. 73, 85, and 73 cells were used in the span-wise direction for the IGV, rotor, and stator, respectively, while 21 span-wise cells were employed into the tip clearance. Fillets were generated using 21 span-wise cells. On the B2B plane, 45, 57, and 53 chord-wise cells were employed for the suction side of the IGV, rotor, and stator, respectively, with an additional 45 cells for the pressure side of all three rows. In the skin block, 37 cells were used to ensure a smooth transition from the wall cell into the main channel. Everywhere, the wall cell size was selected to maintain a maximum y+ lower than 1.2. Further details on the mesh can be found in [26].

4.2. Numerical setup

Unsteady-RANS simulations were solved using a cell-centered finite volume formulation with the FineTurbo 13.2 suite of Cadence. The total pressure distortion described in Section 2 was imposed as inlet boundary condition. This was combined with uniform total temperature measured from clean inlet conditions and a straight axial flow. The inlet turbulence intensity was set to 0.35% (experimentally measured [40]), while the inlet viscosity ratio was assumed to be 50 due to the lack of experimental data, as this is considered a reasonable value for internal flows [41].

Distorted simulations were conducted at the same absolute mass-flow measured for the NS operating point under clean conditions. Thus, the numerical operating point does not correspond to either of the two experimental operating points ($\mathrm{DE}_{d,e}$ and $\mathrm{NS}_{d,e}$) as it aims only to support the description of the distortion propagation mechanisms at an operating point approaching the clean stall boundary. The clean simulations were instead performed at the design mass-flow measured for the clean case. The numerical operating points considered are reported in Table 4.

Speed	**CS (clean)**	**DS (distorted)**
100%	10.00 kg/s	8.45 kg/s ($\mathrm{DE}d,e$)

Table 4 Numerical clean and distorted corrected operating points at 100Nn.

The absolute mass-flow corresponding to these operating points is equal to 11.45 kg/s and 10.04 kg/s for the CS (clean) and DS (distorted) conditions, respectively.

Air was modeled as an ideal gas, with the walls of the numerical domain treated as adiabatic. Time integration was performed through an explicit multi-stage Runge-Kutta method. The Chien $k - \varepsilon$ turbulence model was used, based on the sensitivity analysis conducted in [35]. For the steady numerical setup, mixing plane-type rotor/stator interfaces were employed, along with non-reflective boundaries. For the unsteady numerical setup, instead, 120 time-steps per rotor passage were used to solve accurately up to the $4t\ h$ harmonic of the rotor Blade-Passing-Frequency (BPF).

Simulation results for the distorted case are presented in this paper as normal plots or as a percentage difference between in- stantaneous URANS and steady RANS for the distorted and clean case, respectively. This choice was made because unsteady simula- tions for the clean case were conducted exclusively using a domain scaling approach, preventing the comparison with the full-annulus domain. While subtracting a steady solution from an unsteady one would highlight unsteady flow features through the rotor/stator interfaces (e.g., wakes), it provides valuable insights into the distortion propagation mechanisms.

Figure 7 reports the full-annulus domain used for the simulations. The inlet total pressure boundary condition is highlighted, together with the single-patch outlet.

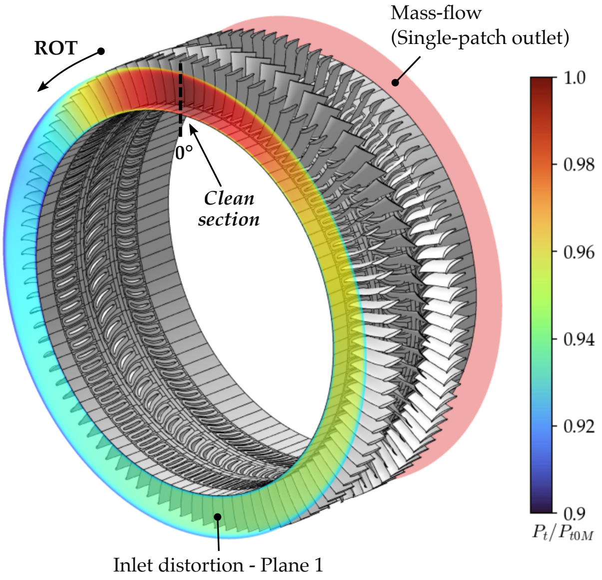

Figure 7 3D full-annulus domain used for the URANS simulations.

5. Results

5.1. Experimental analysis of the stage performance

Figure 8 shows the total-to-total pressure ratio for both the clean and distorted configurations. The compressor map for the distorted case is calculated between the experimental plane downstream of the screen (Plane 1) and the stage outlet (Plane 4) ($\pi tt1 = Pt4M\ /Pt1M\ $), and it is complemented by a contour map of the isentropic efficiency. The corrected mass-flow is also based on the conditions downstream of the screen ($WR1 = Qm\sqrt{(\mathrm{Tt1M\ /Tst\ d\ })}\ /(\mathrm{Pt1M\ /Pst\ d\ })$), and all quantities are non- dimensionalized with respect to the 100Nn design operating point of the clean case ($\pi tt\ d$, WRd). For both configurations, the 100Nn, 96Nn, and 90Nn speeds are considered, and the 95% confidence interval uncertainty is shown.

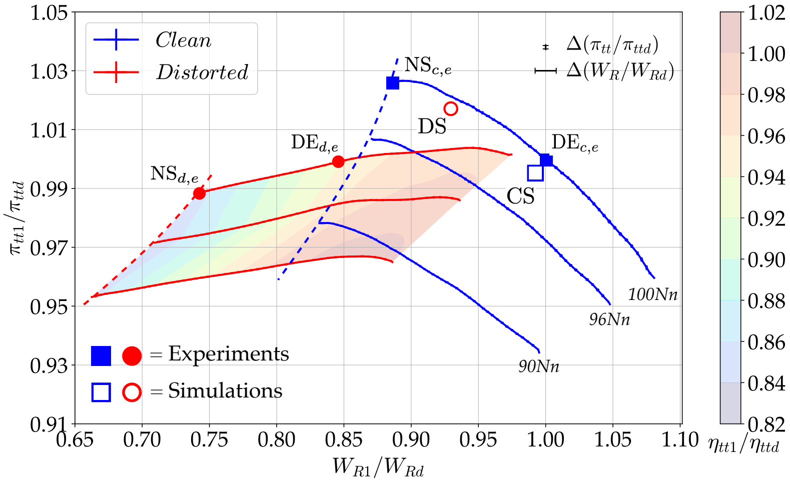

Figure 8 Total-to-total pressure ratio referenced to the screen downstream conditions (Plane 1) at 100Nn, 96Nn and 90Nn.

As already anticipated, this figure demonstrates that the total pressure ratio in distorted conditions decreases at lower mass-flows, extending the operability of the stage beyond the clean stall boundary. Within this regime, losses prevent the outlet total pressure from increasing, suggesting that the machine is partially operating in an unstable manner, even though the typical performance drop of a stalled characteristic is not observed and the operating point remains overall stable. Aerodynamic stall is only detected when the machine is throttled to 75% of the clean design mass-flow at 100Nn. This observation is relevant, as it highlights an extension of stage operability in presence of the distortion, albeit at reduced performance, which is a phenomenon not commonly discussed in the existing literature, at least with regard to traditional compressor designs.

Losses from the screen and the loop limit the achievable mass-flow, with the measured characteristic reaching a maximum of 97.5% of the clean mass-flow at 100Nn. Figure 8 also shows the operating points used for the experimental flow field characterization, corresponding to (DE$_{c,e}$, NS$_{c,e}$) for the DE and NS conditions of the clean case, and (DE$_{d,e}$, NS$_{d,e}$) for the distorted configuration, as reported in Table 2. The simulated clean (CS) and distorted (DS) operating points (Table 4) are also reported.

Figure 9 shows the total-to-total temperature ratio of the stage. Only the 100Nn map is provided, as the same trend applies to reduced speeds.

The plot shows that, unlike the total pressure, the total temperature increases at reduced mass-flows in presence of the distortion. The increased work indicates that the machine does not stall in the traditional sense but presents reduced performance induced by a significant loss increase within the stage. This is confirmed by the efficiency map of Figure 10 and the contour map of Figure 8, which shows more than a 10% efficiency reduction as the mass-flow is decreased.

In conclusion, the distortion appears to extend the stability margin as defined in the classical sense. Contrary to expectations, beyond the clean stability line, the machine does not stall abruptly as it does in the clean configuration but continues to operate, albeit

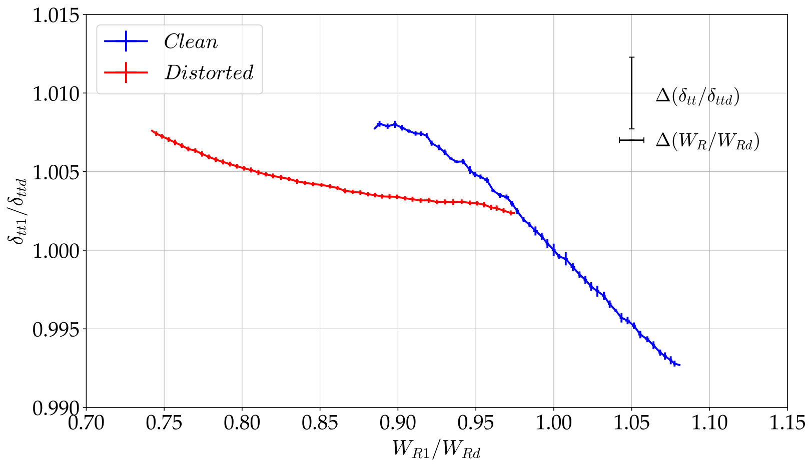

Figure 9 Total-to-total temperature ratio referenced to the screen downstream conditions (Plane 1) at 100Nn.

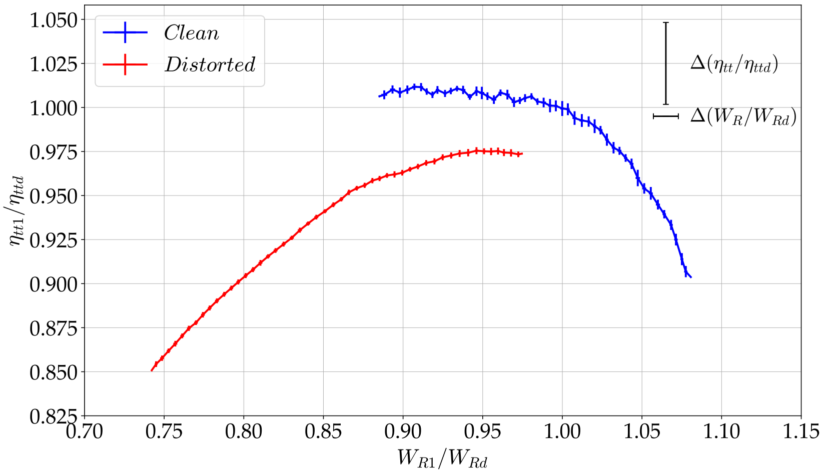

Figure 10 Isentropic efficiency referenced to the screen downstream conditions (Plane 1) at 100Nn.

with reduced performance due to the high losses generated. Aerodynamic stall is encountered only at significantly lower mass-flows. This unexpected operability of the stage motivates the present work, which seeks to identify the critical flow features characterizing thisnewly identified operating regime.

5.2. Experimental characterization of the distortion

Figure 11 shows the total pressure measured in experimental Plane 1 and the percentage difference compared to the reference distortion pattern outlined in Section 2 ($\Delta Pt1 = Pt_{1m} - Pt_{1ref}$), highlighting each distorted sector. This figure corresponds to the design condition of the machine (DE$_{d,e}$).

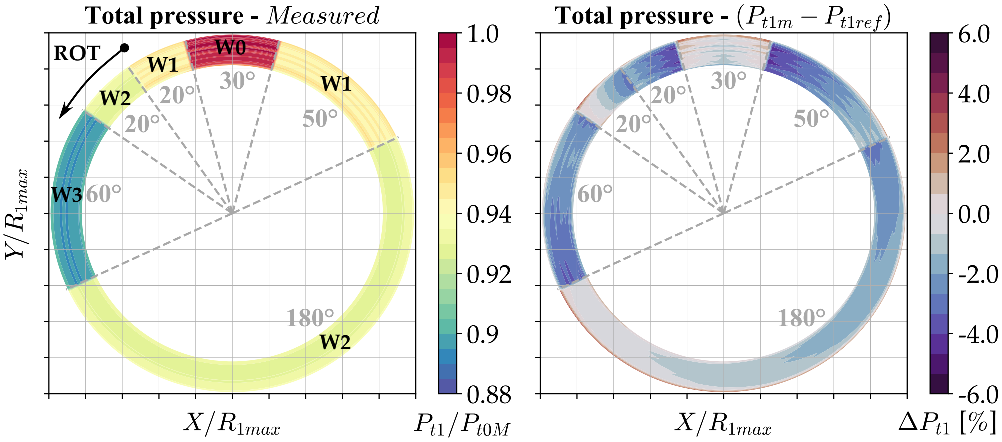

Figure 11 Characterization of the flow field downstream of the distortion screen (Plane 1) at DEd,e 100Nn condition.

This picture shows that the total pressure values in each distorted sector follow the expected order ($Pt_{W0} > Pt_{W1} > Pt_{W2} > Pt_{W3}$). When comparing the measured total pressure to the reference distortion, the maximum difference occurs at the interface between distorted sectors W0 and W1, where a 4.5% difference is observed. This discrepancy results from the reference distortion being a continuous circumferential pattern, while the screen uses discretized sectors. When focusing on the central value of each distorted sector, the maximum deviation is reduced to 3%. It is important to specify that all annular non-uniformities measured within the stage, in

Plane 1 and downstream, originate exclusively from the distortion, with no other contributing sources. This was verified beforehand in the clean stage, where no appreciable inhomogeneities were detected.

Figure 12 shows the total and static pressures, Mach number, and flow angle at DE*d,e* 100Nn conditions, measured downstream of the distortion screen (experimental Plane 1). To improve the visualization of flow quantities, the eight acquired azimuthal positions (distanced 45° apart from each other) have been linearly interpolated over a circumferential grid of 360 points. The DE$_{d,e}$ condition shows that the highest total pressure occurs at the location of the clean region (0° section of Figure 4), corresponding to the total pressure imposed within the loop and measured upstream of the distortion screen (experimental Plane 0). The lowest total pressure is observed between 270° and 315°, coinciding with the distorted sectors W3 and W2, where maximum total pressure loss is expected. Across the circumference, the total pressure gradually decreases, following the reference distortion pattern. This reduction appears to be driven by a decrease in static pressure, particularly pronounced at 315°. As expected, the clean region also exhibits the highest Mach number, while it remains relatively constant elsewhere. Thus, the total pressure distortion results from a combination of Mach number and static pressure distributions. The flow angle reflects the azimuthal static pressure gradient, with flow migrating from high- (90°–225°) to low-pressure regions (at 315°), generating tangential flow. Consequently, counter-clockwise flow (matching the rotor rotation) is observed between 0° and 90°, while clockwise flow (opposite to rotor rotation) appears between 180° and 360°.

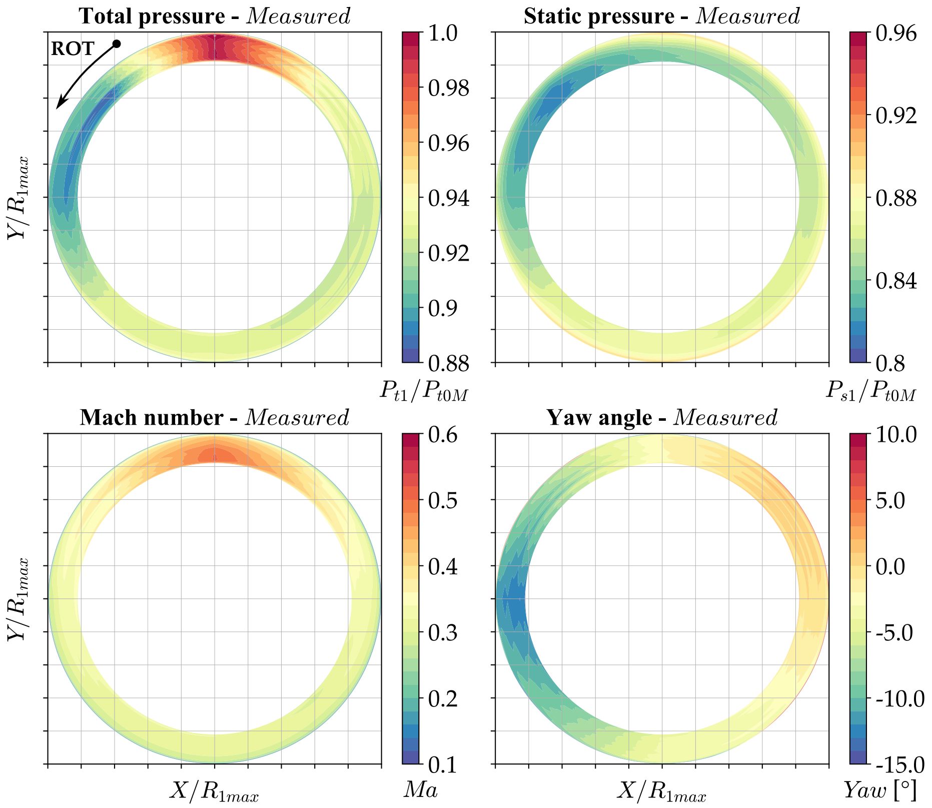

Figure 12 Experimental total pressure, static pressure, Mach number and flow angle downstream of the distortion screen at DEd,e 100Nn condition.

The NS$_{d,e}$ operating point is not reported, as similar trends to the DE$_{d,e}$ condition are observed. However, at reduced mass-flows, a higher flow redistribution and flow angle distortion occur compared to the design condition. It is hypothesized that the increased azimuthal flow redistribution near the stability limit results from a reduction in axial flow momentum.

5.3. Numerical characterization of the distortion propagation downstream of the screen

Figure 13 presents the B2B distributions of total pressure, total temperature and entropy, normalized with the experimental conditions in Plane 0 (stage inlet). The mid-span section was selected to limit the impact deriving from secondary flows located near the end-walls. Moreover, this picture does not show the full 360° to improve visualization, but instead focus around the 0° section, where the clean and maximum distorted regions are visible and most features can be identified. In the picture, the direction of the rotor rotation (ROT) is reported.

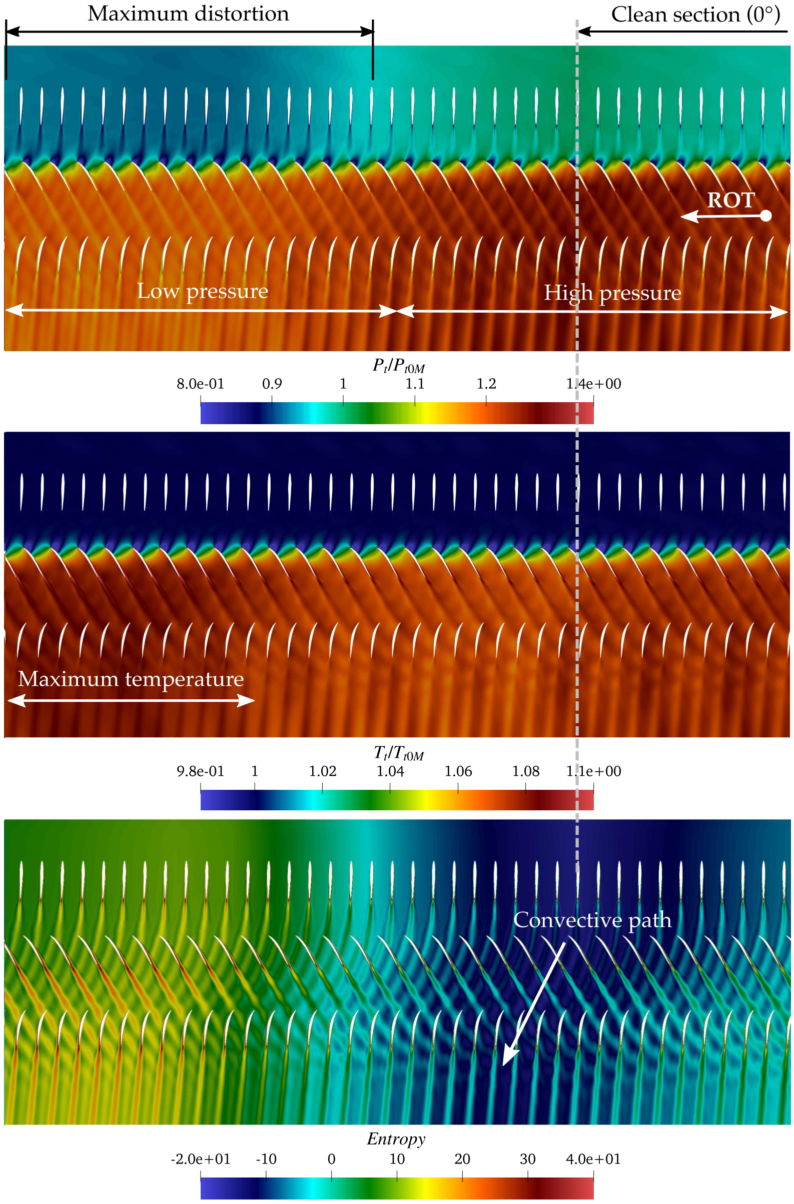

Figure 13 Propagation of total pressure, total temperature and entropy downstream of the screen at 50% span.

Figure 13 highlights the distorted region, characterized by a reduction of total pressure. Downstream, the total pressure increases due to the pressure ratio imposed by the rotor.

No temperature distortion was applied at the inlet, as seen by the constant total temperature across the annulus. However, the reduced axial velocity in the distorted region increases the rotor inlet incidence, enhancing the work input to the rotor. Consequently, a total temperature distortion appears at the outlet, despite the inlet being characterized by constant temperature. The plot also shows that the total temperature distortion is not necessarily aligned with the total pressure one, and a circumferential misalignment exists between the two.

The reduced total pressure, along with constant inlet temperature, causes an entropy increase within the distorted region. The entropy reflects the convective flow path, as it is unaffected by the stream-wise variation of pressure and temperature. The distorted region appears, indeed, shifted in the circumferential direction due to the rotor movement. Considering the equation reported in [42], a circumferential shift of 2 stator pitches was computed.

Figure 14 shows the difference between distorted and clean total pressure, axial velocity, and flow angle. Pressure and velocity are considered as they both influence the flow angle. The total pressure field highlights the clean section and the high- and low-pressure regions. Again, the direction of the rotor rotation (ROT) is highlighted.

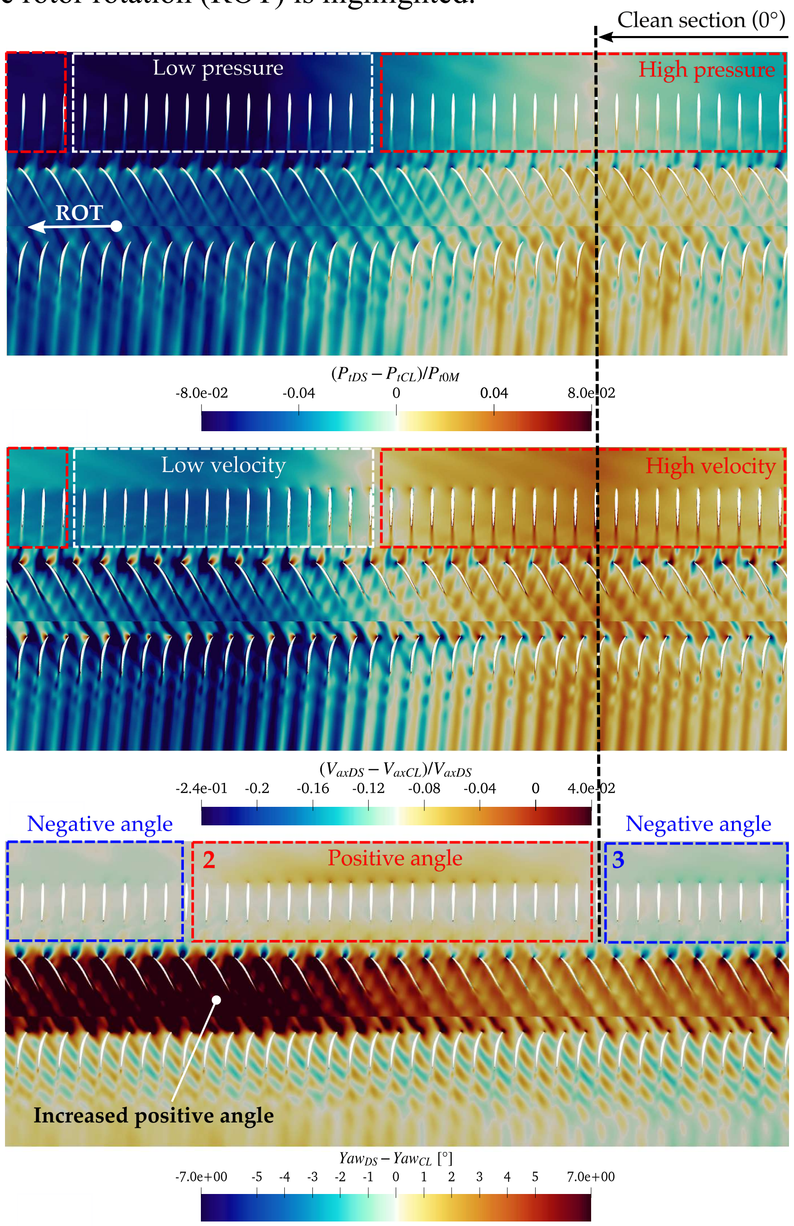

Figure 14 B2B total pressure, axial velocity and flow angle distributions at 50% span: difference between distorted and clean flow field.

In the total pressure field, the clean region shows a zero pressure difference, as the maximum inlet total pressure in the distorted case matches the clean total pressure. Within the clean section, a higher total pressure is observed in the distorted case, indicating a larger pressure ratio in presence of the distortion. This aligns with the fact that the distorted operating point was tested at the same absolute mass-flow as the clean near-stall condition, meaning that the clean section has a pressure ratio similar to the near-stall operating point.

At the inlet section, the axial velocity reflects the total pressure distribution, showing low values where total pressure is reduced. However, in the clean section, the difference between distorted and clean velocities is minimal. This is due to the requirement to maintain the imposed mass-flow, which results in a higher velocity in the clean sector compared to the clean machine. As a result, the clean velocity of the distorted machine closely resembles the velocity observed in the clean stage.

Both axial velocity and static pressure fields define the flow angle. At the inlet section, the flow within the high-pressure region moves toward areas of lower pressure, creating two regions with negative and positive angles (markers 1 and 2 in Figure 14). Following the circumferential pressure gradient, the flow migrates opposite to the rotor rotation within the box labeled *Negative angle* (counter-swirl) and toward the rotor rotation within the box labeled *Positive angle* (co-swirl). As pressure increases and the circumferential gradient reverses, counter-swirl occurs (marker 3). However, the flow straightens through the IGV, with the flow angle reducing from 1.5° upstream of the IGV to 1° upstream of the rotor in the maximum co-swirl regions. The axial velocity distortion amplifies the flow angle distortion. In the region of low axial velocity, intense co-swirl flow is observed, increasing the absolute tangential velocity at the rotor outlet. At the stage outlet, the flow angle rises due to the axial velocity reduction, differing from the clean values by 1° on average.

The flow angle distribution helps explaining the total temperature variation shown in Figure 13. In Figure 15, based on the combination of flow angle and axial velocity, four distinct regions over the annulus can be identified: 1) Counter-swirl flow with low axial velocity (red); 2) Co-swirl flow with low axial velocity (green); 3) Co-swirl flow with high axial velocity (yellow); and 4) Counter-swirl flow with high axial velocity (blue). The clean velocity triangle is shown in gray.

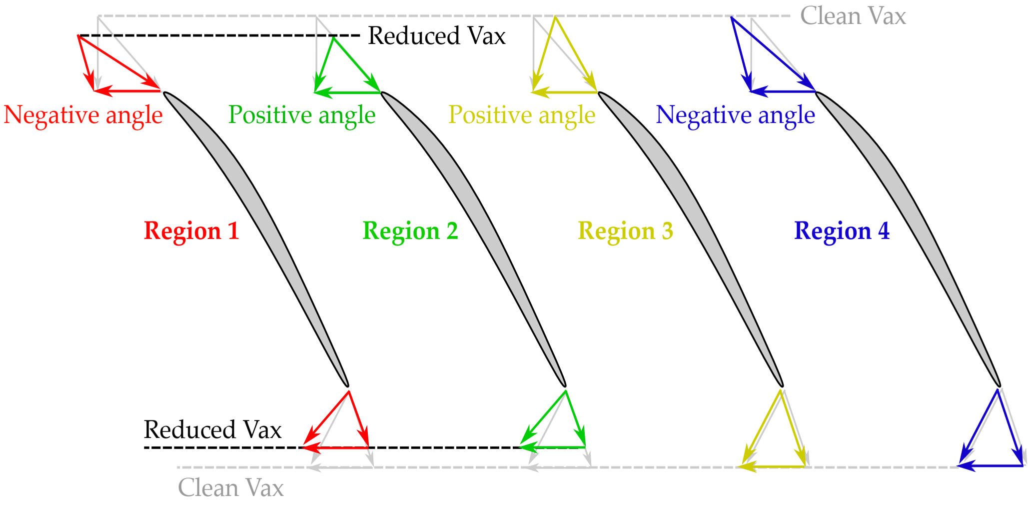

Figure 15 Schematic of the velocity triangles around the annulus.

Using the definition of Euler work: $W = u \cdot (v_{\theta 2} - v_{\theta 1})$, the circumferential location where the highest work is performed can be identified. Specifically, Region 1 exhibits the highest $v_{\theta 2}$ and $v_{\theta 1} < 0$, thereby maximizing the work performed by the rotor and hence the total temperature at the rotor outlet. Note that Figure 15 does not account for the impact of the inlet incidence on the deviation angle and, consequently, the absolute flow angle at the rotor outlet. Nevertheless, it offers a simplified yet useful visualization of the overall total temperature distortion behavior.

This observation is further supported by Figure 16, showing the total temperature difference between distorted and clean case. The total temperature difference at the inlet section is zero throughout, as the imposed temperature is the same in both clean and distorted conditions with no distortion applied. However, as the flow moves across the rotor, a total temperature distortion arises due to the non-uniform work distribution. From the analysis of the velocity triangles, Region 1 is identified as the azimuthal location where the highest work is performed. This region also corresponds to the point of maximum total temperature, as shown in Figure 13 and Figure 16.

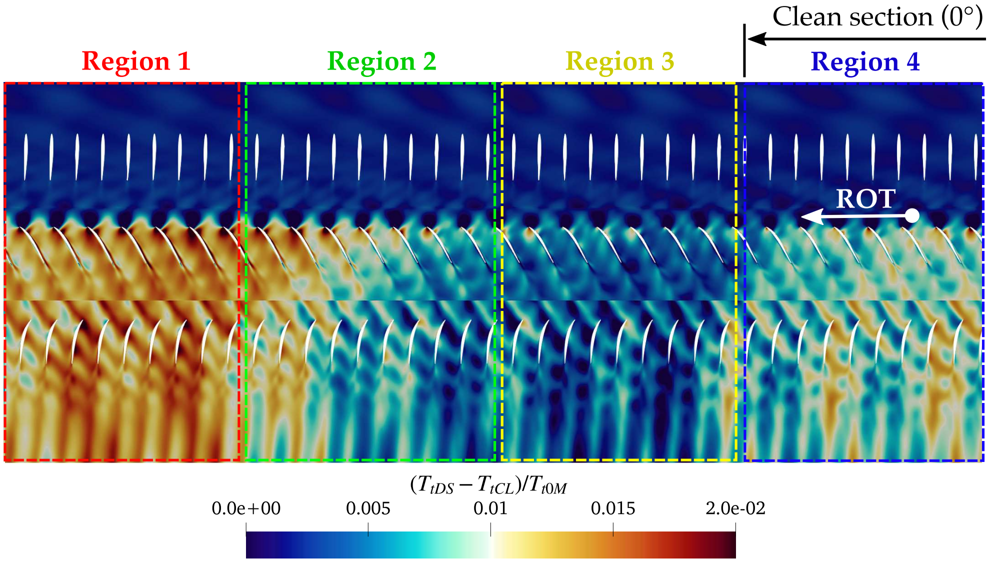

Figure 16 B2B total temperature distribution at 50% span: difference between distorted and clean flow field.

5.4. Numerical characterization of the circumferential distortion migration

To characterize the distortion propagation through the rotor, Figure 17 shows the circumferential distributions at mid-span for the IGV inlet (Plane 1 - *in*) and the rotor outlet (Plane 3 - *out*), shown with full and empty markers, respectively. The quantities are normalized using the maximum and minimum values computed at the inlet. This removes the stream-wise variation, while highlighting the attenuation relative to the inlet section. The flow quantities are extracted at a relative azimuthal distance of one stator pitch.

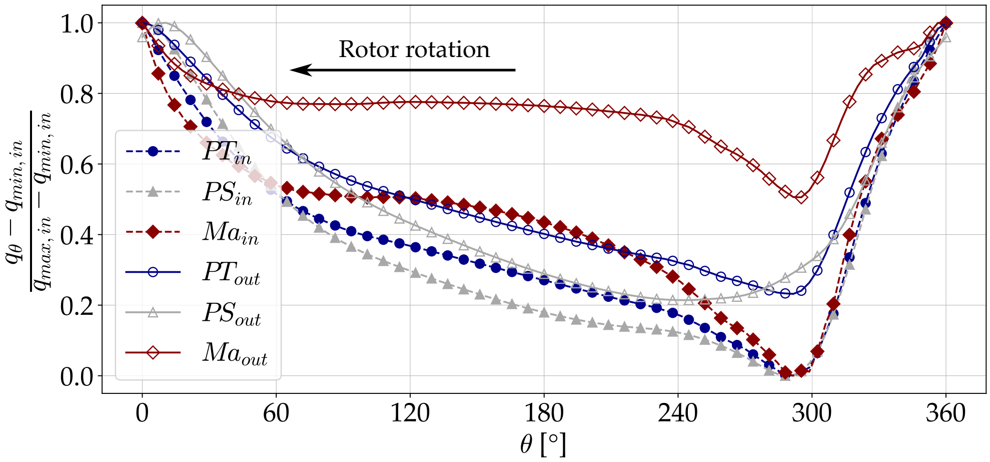

Figure 17 Total pressure, static pressure and Mach number mid-span distributions at the stage inlet (Plane 1 - *in*) and rotor outlet (Plane 3 - *out*) around the annulus.

Figure 17 shows that, compared to the inlet section, the distortion is attenuated at the rotor outlet for both pressure and Mach number, as indicated by the difference between maximum and minimum values. To analyze the total pressure distribution, static pressure and Mach number are examined first.

The static pressure is expected to increase across the entire annulus as the flow passes through the rotor. However, regions with higher loading and rotor work will experience a higher increase in static pressure. As a result, static pressure in the clean region rises, though at a lower rate than in other circumferential locations. This reduces the difference between maximum and minimum static pressure at the rotor outlet. The largest increase occurs at 290°, coinciding with the minimum total pressure and maximum total temperature location. This shifts the minimum static pressure to around 240°. Additionally, the maximum static pressure shifts by two stator pitches opposite to the rotor rotation. While the precise cause is unclear, in [42] it was noted that the speed of sound, typically higher than the convective speed, may contribute to the propagation of static pressure distortion in the direction of the rotor stagger.

The Mach number follows a similar trend compared to the static pressure. Although an increase in absolute Mach number is expected across the annulus as the flow passes through the rotor, the highest rise occurs in the highly distorted region. This increase in Mach number in distorted regions is likely due to higher loading and static pressure ratios in those regions. Overall, this effect reduces the velocity distortion at the rotor outlet.

The total pressure profile is thus obtained combining the static pressure and Mach number distributions, resulting in an overall increase in total pressure, particularly in the most distorted regions. The decoupling of static pressure and velocity distortions, no longer aligned at the same circumferential location, appears to contribute to smoothing the total pressure distortion at the rotor outlet.

5.5. Experimental characterization of the circumferential distortion migration

To assess the circumferential migration of the distortion induced by the rotor, Figure 18 shows the experimental total pressure and temperature at the rotor outlet. Only the design condition (DE*d*,*e*) is shown, as similar conclusions hold at near-stall. Every quantity has been expressed as percentage between maximum and minimum values, so that the circumferential variation of the pressure and temperature is highlighted.

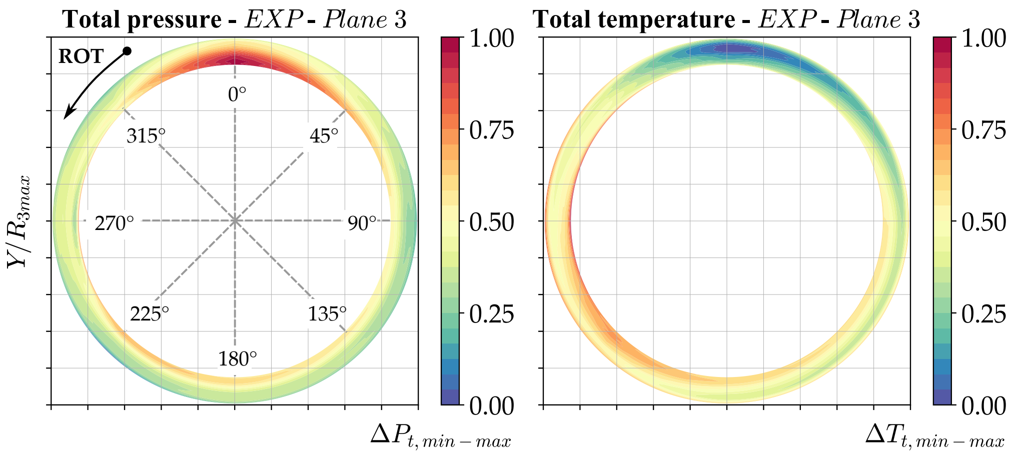

Figure 18 Experimental map of total pressure and total temperature at the rotor outlet at DEd,e 100Nn condition.

From the figure, the maximum total pressure remains at 0°, consistent with the IGV inlet (Plane 1). However, the rotor outlet total pressure distortion spreads across a larger portion of the annulus compared to the inlet, with total pressure remaining relatively constant except for 0°. Additionally, total pressure is higher near the hub wall due to the rotor loading and work delivered at low span. A tentative explanation for the flow redistribution and distortion attenuation downstream of the rotor was provided in the previous paragraph. As a consequence of the non-uniform circumferential work distribution on the rotor, a total temperature distortion appears at the rotor outlet even though the inlet total temperature is uniform, as shown in Figure 18 and highlighted from the results of the simulations.

To better visualize the pressure and temperature variation around the annulus, Figure 19 shows the experimental total pressure and temperature at mid-span as a function of the azimuthal position. The values are normalized as percentages of the maximum and minimum. The azimuthal location follows the same reference as in Figure 18, oriented opposite to the rotor rotation.

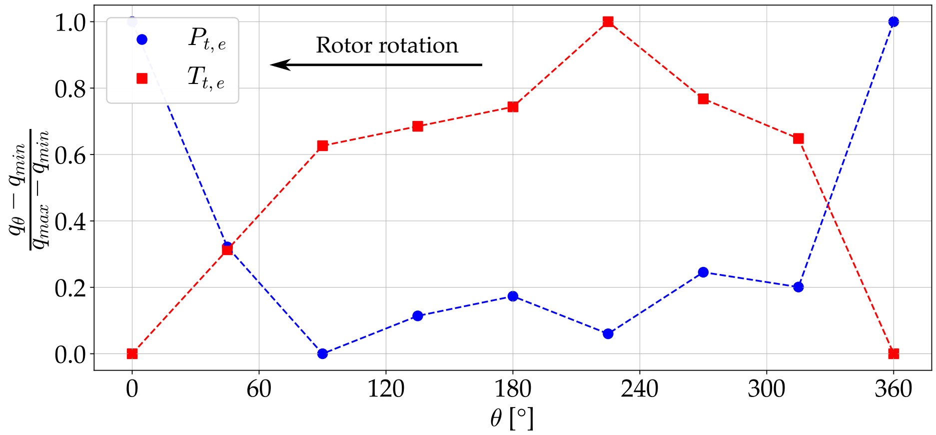

Figure 19 Experimental mid-span distributions of total pressure and total temperature at the rotor outlet around the annulus.

As shown in the figure, the maximum total pressure occurs at 0°. However, it rapidly decreases to the minimum within the first 90° and remains below 25% up to 315°. It should be noted that the azimuthal resolution of the experiments (45°) may limit the identification of the precise location of the maximum and minimum pressures.

The same trend is observed for the total temperature. The maximum temperature occurs at 225°. Moving away from the clean region, there is an increase in total temperature, followed by a plateau between 60°-180°. After reaching the maximum, a sharp drop occurs, with the minimum at 360°. Again, the limited azimuthal resolution of the experiments may result in the minimum total temperature being located at a different position than 0°. However, this distribution remains physically consistent, as reduced work is expected near the clean sector.

In conclusion, as the flow advances through the rotor, the total pressure distortion is attenuated. The only new component emerging is the distortion of total temperature.

5.6. Secondary flows induced by the distortion

5.6.1. Experimental evidence at the rotor outlet

Figure 20 reports the experimental span-wise distributions of total pressure and absolute flow angle at the rotor outlet, for all the acquired azimuthal positions. The total pressure has been expressed as reduction with respect to the clean conditions at mid-span. Data from probe traversing performed in clean conditions are also included for reference.

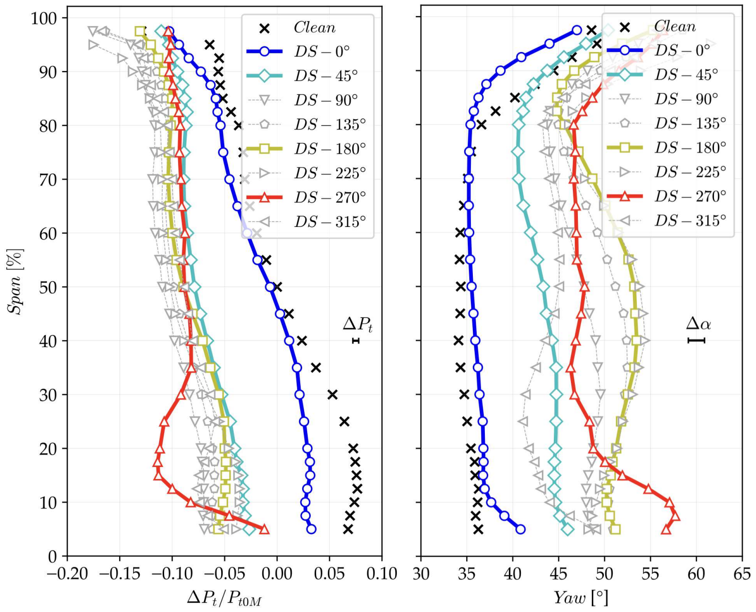

Figure 20 Total pressure and Yaw angle span-wise distributions at the rotor outlet at DEd,e 100Nn.

Figure 20 shows that at 0° (corresponding to the clean section), the total pressure is maximum and aligns with the clean distribution, particularly for spans greater than 40%. However, a 3.5% mismatch in total pressure is observed at 15% span and 2.5% at the tip. This phenomenon is attributed to variations in the size and intensity of secondary structures near the end-walls. The 0°, 45°, 180°, and 270° positions, corresponding to distorted sectors with different pressure losses, are highlighted with colors, while all other positions are shown in gray. As observed in the circumferential pressure distribution at mid-span, all positions except 0° exhibit similar pressure values across most of the blade span. However, a notable pressure drop is seen at 270° for spans below 30%, indicating an intensified hub corner flow. This azimuthal location coincides with the area of maximum pressure deficit and minimal axial velocity, where increased incidence amplifies the size and intensity of the corner flow.

These observations are supported by the flow angle. At 0°, the clean distribution closely matches the flow away from the end-walls, with a maximum difference of 5° compared to the clean case. At mid-span, a 1.5° difference is observed in the clean section, increasing to 12.3°

at the 270° section. The marked hub corner separation is confirmed by the flow angle increase below 30% span at 270°, reaching an absolute value of 57.6°.

To highlight the difference between clean and distorted regions, Figure 21 shows the pressure PLA and RMS for the clean case, along with the distorted regions at 0° and 270°, where higher and lower inlet total pressures occur. The total pressure at mid-span is removed to improve visibility, otherwise the picture would scale with the local pressure ratio corresponding to the specific annular section considered.

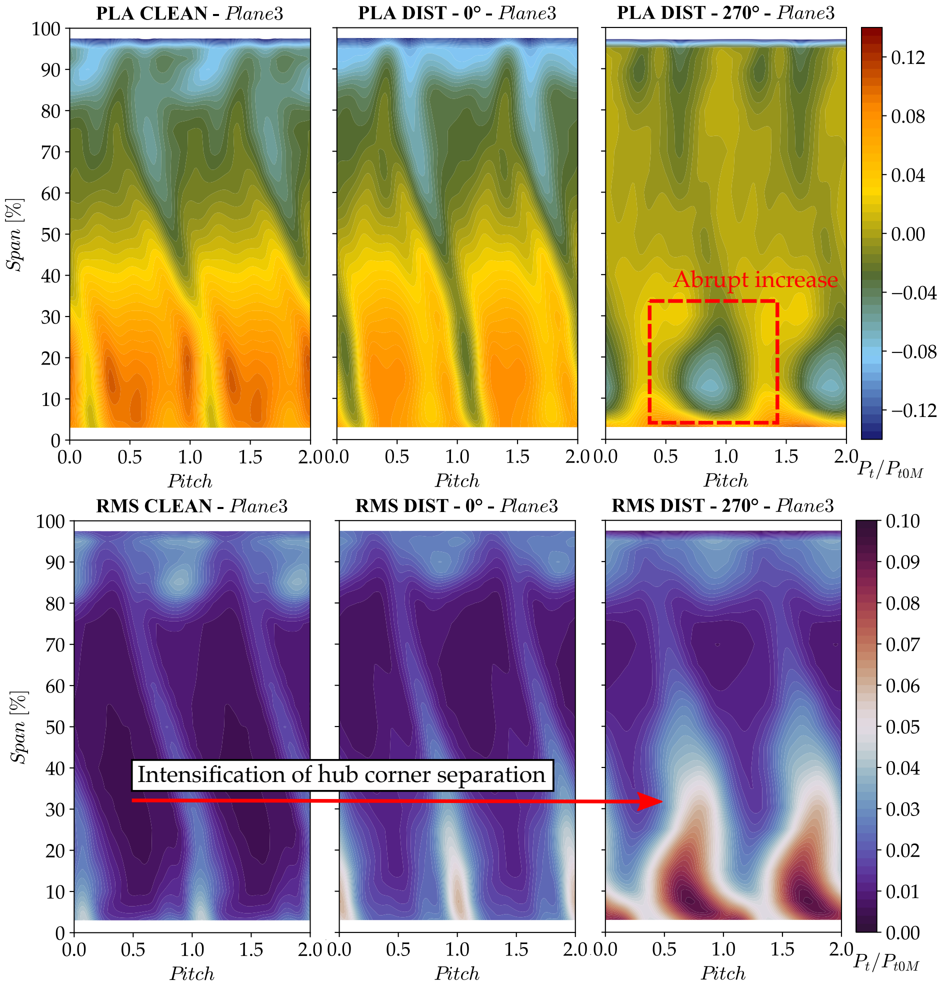

Figure 21 Total pressure PLA (top) and corresponding RMS (bottom) for clean and distorted configurations (0° and 270° azimuthal positions) at the rotor outlet.

As seen in the span-wise distribution of total pressure, the PLA shows that, compared to the clean case, the distorted 0° location features a thicker wake across most of the blade span. At 270°, an abrupt increase in corner separation size and intensity is observed, extending over nearly 50% of the blade pitch and 30% of the span. The intensified hub corner separation contributes to the total pressure reduction near the hub wall, a trend that is even more pronounced in the pressure fluctuation. In clean conditions, the core of the hub separation has an RMS equal to 0.04. However, in the highly distorted regions, the fluctuation increases to about 10% of the inlet total pressure, spanning most of the rotor pitch. At the tip, the span-wise extent of the tip-leakage flow appears relatively constant within the distorted regions.

This analysis highlights that in the distorted configuration the flow re-adaptation forces the low-distorted regions to behave like the clean machine, and the highly-distorted regions to develop critical flow features near the hub wall. This supports the idea that the machine is not stalled in the classical sense within the considered operating range but suffers from reduced operability due to intensified flow structures developing in the distorted portion of the annulus. It is hypothesized that in the distorted region, the hub separation does not evolve into stall due to the limited azimuthal extent of the distortion, which is surrounded by less distorted regions where such structures do not develop. However, this observation requires further investigation.

5.6.2. Experimental evidence at the stator outlet

Figure 22 reports the stage outlet total pressure, where the pitch-wise average at mid-span was removed from the plots to enhance visibility. In Figure 23 instead, the span-wise pressure gradient has been removed. The angles 0°, 45°, and 270° were selected to emphasize the behavior of a low-distorted (45°) and highly distorted (270°) regions compared to the clean sector (0°).

The figure shows that the clean sector (0°) presents reduced corner flows and wake thickness. Moving to other regions of the

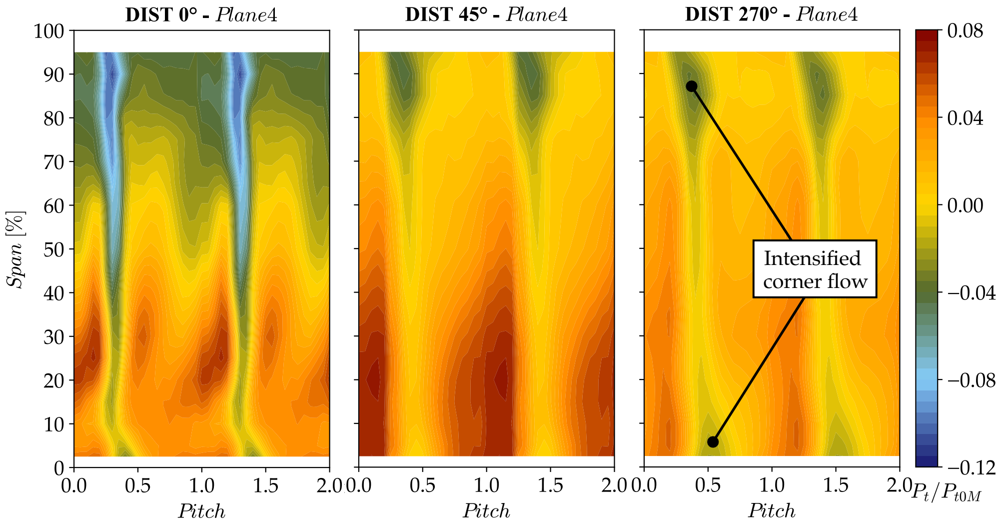

Figure 22 Stage outlet total pressure in distorted conditions at 0°, 45° and 270°: Pressure normalized with pitch-wise average at mid-span at DEd,e 100Nn.

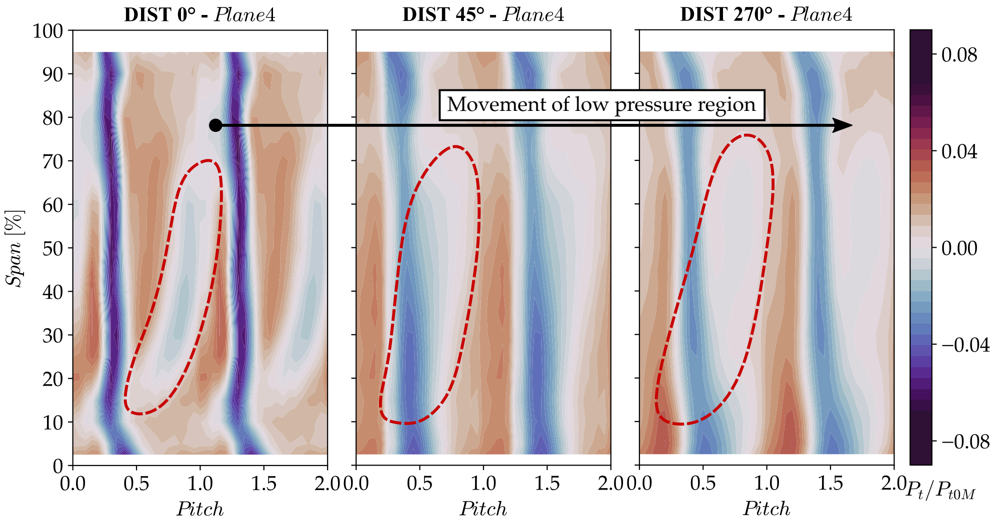

Figure 23 Stage outlet total pressure in distorted conditions at 0°, 45° and 270°: Pressure normalized with pitch-wise span average at DEd,e 100Nn.

annulus, the tip and hub corner flows become significantly stronger, especially at 270°, where the distortion is most pronounced. As predicted from the rotor analysis, this enhancement of flow structures at the stator end-walls is influenced by two factors: 1) In the distorted region, an increase in the absolute flow angle at the rotor outlet alters the stator inlet incidence; 2) The rotor flow field analysis shows a marked intensification, particularly of the hub corner separation, as the distortion increases. This leads to a local flow blockage, further reducing axial velocity and intensifying the incidence near the hub wall.

Figure 23 also highlights a low total pressure region in the middle of the stator passage. Analysis of the clean machine shows that this low-pressure region results from the propagation of upstream IGV wakes, with its location varying depending on the operating point. For further information about the characterization of the clean machine refer to [26]. At the 0° location (clean sector), indeed, the reduced pressure region aligns with the clean machine. In more distorted sectors, the IGV wake propagates through a different portion of the stator passage and partially interacts with the stator blade. At 45°, the wake thickness increases due to interaction with the upstream IGV wake. At 270°, a further azimuthal shift of this region decreases the wake thickness at 50% span but intensifies the hub corner flow. The hub corner flow appears enhanced by increased inlet incidence and interaction with the upstream IGV wakes. The propagation phenomena of this reduced pressure region when throttling the machine was already explained and discussed in [26].

Overall, the clean sector of the distorted machine behaves similarly to the clean machine. However, in the distorted region, the machine operates like the clean machine near the stability limit. This suggests that, while the machine remains stable, certain portions of the annulus promote the development of critical flow structures due to increased rotor inlet incidence.

6. Conclusion

This paper presented an experimental and numerical study conducted on a 1.5-stage low-pressure compressor, representative of the first stage of a modern booster, subjected to an inlet distortion replicating the fan outlet flow field in an UHBR engine operating in crosswind conditions.

The performance analysis revealed that both the pressure ratio and compressor efficiency are significantly affected by the inlet distortion. Contrary to expectations, the distortion appears to extend the stall margin of the stage without leading to aerodynamic stall beyond the clean stall boundary.

The experimental results support the idea that the rotor is significantly unbalanced due to the high circumferential redistribution occurring upstream. This flow reorganization determines a strong unbalance between the clean and the distorted regions, promoting critical flow mechanisms within the highly distorted areas. The rotor hub corner separation emerges as the primary mechanism influencing the stage stability.

The development of these flow mechanisms in the highly distorted regions of the annulus is believed to promote a critical operation of the stage, resulting in increased losses, as observed in the stage performance. However, this effect seems counterbalanced by the clean region, where flow disturbances are small and similarto those of the clean machine. The high inlet flow redistribution, combined with the development of critical flow structures in the distorted regions, possibly allows for a reduced yet stable performance of the stage beyond the clean stall boundary. It is hypothesized that the hub separation does not evolve into stall because the distorted region is surrounded by less disturbed areas, thereby limiting the development of a stall cell. Future activities should explore the existence of a critical distortion extent and intensity at which the same machine stalls. Additionally, it should be investigated how a specific distortion, when applied to two different machines, could either induce or prevent stall, depending on the aerodynamic design of the stage.

Unlike typical cases where the distortion reduces the compressor stall margin, this paper highlights a modification of stage operability when the compressor operates beyond its clean stall boundary. This observation could potentially lead to a redefinition of design guidelines, or a revision of the stall margin definition to account for extended operability at reduced performance. The findings from this study are believed to provide valuable insights for designers, as modern compressors may be capable of operating for short periods beyond the clean stall limit at reduced performance without expe- riencing aerodynamic stall. These results are expected to stimulate further analysis and generate interest within the broader engine community.

Acknowledgments

The authors would like to express their gratitude to Remy Princivalle for the valuable insights provided throughout the duration of the project. They also thank Safran Aero Boosters to make the DREAM compressor stage available for this study, and Cadence to grant access to the simulation software. The CÉCI consortium is acknowledged for providing access to the Tier-1 Lucia cluster. Additionally, the authors thank the F.R.S.-FNRS for funding the FRIA scholarship of Riccardo Toracchio.

Nomenclature

Acronyms

UHBR = Ultra-High ByPass Ratio
IGV = Inlet Guide Vane
NS = Near-Stall
DE = DEsign
PLA = Phase-Locked-Average
RMS = Root-Mean-Square
BPF = Blade-Passing-Frequency
B2B = Blade-to-Blade
CS = Clean Simulated operating point
DS = Distorted Simulated operating point

Roman letters

K = Loss coefficient
D = Stage external diameter
W = Wire screen sector, Euler work
WR = Corrected mass-flow
Nn = Percentage of corrected speed
q = General flow quantity

Greek Letters

θ = Circumferential location
β = Screen porosity
π = Pressure ratio
Δ = Uncertainty, difference
δ = Temperature ratio
η = Isentropic efficiency

Dimensionless Groups

Re = Reynolds number

Superscripts and subscripts

t = Total quantity
0 = Quantity computed in Plane 0
M = Area-averaged quantity
e = Experimental operating point
c = Clean operating point
d = Distorted operating point, design
dw = Wire diameter
C = Coefficient from catalog
std = Standard quantity
4 = Quantity computed in Plane 4
1 = Quantity computed/referenced to Plane 1
tt = Total-to-total quantity
s = Static quantity
in = Inlet quantity
out = Outlet quantity

References

[1] Peters, A., Spakovszky, Z., Lord, W., and Rose, B., 2015, “Ultrashort Nacelles for Low Fan Pressure Ratio Propulsors,” Journal of Turbomachinery, 137(2).

[2] Mohankumar, B., Hall, C., and Wilson, M., 2021, “Fan Aerodynamics With a Short Intake at High Angle of Attack,” Journal of Turbomachinery, 143(5).

[3] Mohankumar, B., Hall, C., and Wilson, M., 2022, “Sweep Effects on Fan–Intake Aerodynamics at High Angle of Attack,” Journal of Turbomachinery, 144(10).

[4] Uranga, A., Drela, M., Hall, D., and Greitzer, E., 2018, “Analysis of the Aerodynamic Benefit From Boundary Layer Ingestion for Transport Aircraft,” AIAA journal, 56(11).

[5] Plas, A., Sargeant, M., Madani, V., Crichton, D., Greitzer, E., Hynes, T., and Hall, C., 2007, “Performance of a Boundary Layer Ingesting (BLI) Propulsion System,” 45th AIAA aerospace sciences meeting and exhibit.

[6] Gunn, E., Tooze, S., Hall, C., and Colin, Y., 2013, “An Experimental Study of Loss Sources in a Fan Operating With Continuous Inlet Stagnation Pressure Distortion,” Journal of Turbomachinery, 135(5).

[7] Perovic, D., Hall, C., and Gunn, E., 2019, “Stall Inception in a Boundary Layer Ingesting Fan,” Journal of Turbomachinery, 141(9).

[8] Taghavi Zenouz, R., Eshaghi Sir, M., and Ababaf Behbahani, M., 2017, “Performance of a Low Speed Axial Compressor Rotor Blade Row Under Different Inlet Distortions,” Mechanical Sciences, 8(1).

[9] Reid, L. and Moore, R., 1978, “Design and Overall Performance of Four Highly Loaded, High Speed Inlet Stages for an Advanced High-Pressure-Ratio Core Compressor,” NASA Technical Report.

[10] Strazisar, A., Wood, J., Hathaway, M., and Suder, K., 1989, “Laser Anemometer Measurements in a Transonic Axial-Flow Fan Rotor,” NASA Technical Report.

[11] Fidalgo, V., Hall, C., and Colin, Y., 2012, “A Study of Fan-Distortion Interaction Within the NASA rotor 67 Transonic Stage,” Journal of Turbomachinery, 134(5).

[12] Zhang, W. and Vahdati, M., 2019, “A Parametric Study of the Effects of Inlet Distortion on Fan Aerodynamic Stability,” Journal of Turbomachinery, 141(1).

[13] Yang, B. and Zhu, G., 2023, “Impacts of Inlet Circumferential Distortions on the Aerodynamic Performance of a Transonic Axial Compressor,” Processes, 11(7).

[14] Lesser, A. and Niehuis, R., 2014, “Transonic Axial Compressors With Total Pressure Inlet Flow Field Distortions,” Turbo Expo: Power for Land, Sea, and Air.

[15] Zhang, W., Stapelfeldt, S., and Vahdati, M., 2020, “Influence of the Inlet Distortion on Fan Stall Margin at Different Rotational Speeds,” Aerospace Science and Technology, 98.
[16] Zhang, W. and Vahdati, M., 2020, “Stall and Recovery Process of a Transonic Fan With and Without Inlet Distortion,” Journal of Turbomachinery, 142(1).
[17] Yang, Z., Lu, H., Pan, T., and Li, Q., 2021, “Numerical Investigation on the Influences of Boundary Layer Ingestion on Tip Leakage Flow Structures and Losses in a Transonic Axial Flow Fan,” Journal of Fluids Engineering, 143(11).
[18] Barthmes, S., Haug, J., Lesser, A., and Niehuis, R., 2016, “Unsteady CFD Simulation of Transonic Axial Compressor Stages With Distorted Inflow,” Symposium on Field of the Research Unit 1066.
[19] Castillo, P. and Hall, C., 2021, “Aerodynamics of Boundary Layer Ingesting Fuselage Fans,” Journal of Turbomachinery, 143(4).
[20] Castaneda, J., Mehdi, A., Di Cugno, D., and Pachidis, V., 2011, “A Preliminary Numerical CFD Analysis of Transonic Compressor Rotors When Subjected to Inlet Swirl Distortion,” Turbo Expo: Power for Land, Sea, and Air.
[21] Hah, C., Rabe, D., Sullivan, T., and Wadia, A., 1998, “Effects of Inlet Distortion on the Flow Field in a Transonic Compressor Rotor,” Journal of Turbomachinery, 120(2).
[22] Soderquist, D., Gorrell, S., and Custer, C., 2018, “Analysis of Distortion Transfer and Generation Through a Compressor Using the Harmonic Balance Approach,” AIAA Aerospace Sciences Meeting.
[23] Reid, C., 1969, “The Response of Axial Flow Compressors to Intake Flow Distortion,” ASME Gas Turbine Conference and Products Show.
[24] “Safran Private Communication,” .
[25] Dickens, T. and Day, I., 2011, “The Design of Highly Loaded Axial Compressors,” Journal of Turbomachinery, 133(3).
[26] Toracchio, R., Fontaneto, F., and Hillewaert, K., 2023, “Steady and Unsteady Numerical Characterization of the Secondary Flow Structures of a Highly Loaded Low-Pressure Compressor Stage,” International Journal of Turbomachinery, Propulsion and Power, 8(4).
[27] Hadavandi, R., Fontaneto, F., and Desset, J., 2018, “Complete Characterization of a Highly Loaded Low Pressure Compressor at Different Reynolds Numbers for Computational Fluid Dynamics Simulations,” Journal of Turbomachinery, 140(6).
[28] Dell’Era, G., Habotte, N., Desset, J., Brouckaert, J., and Hiernaux, S., 2015, “Experimental Characterization of Stall Phenomena in a Single-Stage Low-Pressure Axial Compressor,” Journal of Power and Energy, 229(5).
[29] Sans, J., Dell’Era, G., Desset, J., Brouckaert, J., and Hiernaux, S., 2013, “Time-Resolved Measurements of the Unsteady Flow Field in a Single Stage Low Pressure Axial Compressor,” Turbo Expo: Power for Land, Sea, and Air.
[30] Wieghardt, K., 1953, “On the Resistance of Screens,” Aeronautical Quarterly, 4(2).
[31] Gunn, E. and Hall, C., 2014, “Aerodynamics of Boundary Layer Ingesting Fans,” Turbo Expo: Power for Land, Sea, and Air.
[32] Gaetani, P. and Persico, G., 2020, “Technology Development of Fast-Response Aerodynamic Pressure Probes,” International Journal of Turbomachinery, Propulsion and Power, 5(2).
[33] Mersinligil, M., Brouckaert, J., and Desset, J., 2011, “Unsteady Pressure Measurements With a Fast Response Cooled Probe in High Temperature Gas Turbine Environments,” Journal of Engineering for Gas Turbine and Power, 133(8).
[34] ASME, 2006, “ANSI/ASME PTC 19.1-2005 Measurement uncertainty,” American Society of Mechanical Engineers.

[35] Toracchio, R., Fontaneto, F., and Hillewaert, K., 2022, “On the Impact of the Turbulence Model on the Secondary Flow Structure of a Highly-Loaded Compressor Stage,” Turbo Expo: Power for Land, Sea, and Air.
[36] Babin, C., Dumas, M., Ottavy, X., and Fontaneto, F., 2021, “Numerical Characterisation of a HP Compressor Stage Equipped With a Closed Shrouded Stator Cavity,” Journal of Turbomachinery, 147(4).
[37] Babin, C., Ottavy, X., and Fontaneto, F., 2023, “Leakage Flow Impact on Shrouded Stator Cavity Flow Topology and Associated High-Speed Axial Compressor Stage Performance,” Journal of Turbomachinery, 145(5).
[38] Roache, P., 1994, “Perspective: A Method for Uniform Reporting of Grid Refinement Studies,” Journal of Fluids Engineering, 116(3).
[39] Celik, I., Ghia, U., Roache, P., and Freitas, C., 2008, “Procedure for Estimation and Reporting of Uncertainty Due to Discretization in CFD Applications,” Journal of Fluids Engineering, 130(7).
[40] Hadavandi, R., 2016, “Experimental Investigation of the Inlet Flow Field on a Highly Loaded Single Stage Low Pressure Axial Compressor,” VKI Project Report.
[41] Numeca International, 2019, Fine/Turbo Theory Guide, 13th ed.
[42] Mazzawy, R., 1977, “Multiple Segment Parallel Compressor Model for Circumferential Flow Distortion,” Journal of Engineering for Gas Turbine and Power, 99(2)

List of Figures

List of Tables